Journal of ELECTRONIC MATERIALS, Vol. 44, No. 2, 2015
DOI: 10.1007/s11664-014-3528-0

Thermal Stress of Surface Oxide Layer on Micro Solder Bumps During Reflow

C. KEY CHUNG,[1,3] Z.X. ZHU,[2] and C.R. KAO[2,4]

1.—Intel Microelectronics Asia Ltd, Taipei, Taiwan. 2.—Department of Materials Science and Engineering, National Taiwan University, Taipei, Taiwan. 3.—e-mail: chee.key.chung@intel.com. 4.—e-mail: crkao@ntu.edu.tw

Micro-bumps are now being developed with diameters smaller than 10 μm. At these dimensions, only very small amounts of solder are used to form the interconnections. Surface oxidation of such small micro-bumps is a critical issue. The key question is whether the oxide film on the solder bumps acts as a barrier to formation of solder joints. In this work, the mechanical stability of the oxide layer on solder bumps was investigated. Solder bumps with 35-μm radii were heated for different times. Auger electron spectroscopy was used to determine the thickness of the oxide layer on the solder bumps. Solder bumps with known oxide layer thicknesses were then heated in a low-oxygen environment (<50 ppm) until they melted. The mechanical stability of the oxide layer was observed by use of a high-speed camera. Results showed that a 14-nm-thick oxide layer on a solder bump of radius 35 μm was able to withstand the molten solder without cracking, leading to a non-wetting solder joint. A thermal stress model of the surface oxide layer revealed that the stress varied substantially with bump size and temperature, and increased almost linearly with temperature. Upon melting, the thermal stress on the oxide increased abruptly, because of the higher thermal expansion of molten solder compared with its solid state. On the basis of the experimental results and the thermal stress model of the oxide film, the maximum oxide thickness that can be tolerated to form a solder joint was determined, e.g. 14 nm oxide can support liquid solder, and thus lead to a non-wetting condition. This work provided a new method of determination of the maximum stress of oxide film for solder joint formation.

Key words: Surface oxidation, micro solder bump, fracture, soldering, wetting, thermal stress

INTRODUCTION

The sizes and pitches of micro-bumps on Si dies continue to decrease. The recent use of through-silicon-via interconnects enables the sizes and pitches of micro-bumps to shrink to 10 and 25 μm, respectively.[1,2] At these dimensions, only very small amounts of solder are needed to form the interconnection. As the size of the solder bump decreases, the oxide layer on the solder becomes more resistant to reflow. In addition, the probability of non-wetting for these tiny solder joints also increases. Thus, an oxide-free solder bump surface is essential to establishing reliable solder interconnects.

In our earlier work we investigated Cu oxide-induced non-wetting of solder joints. It was found that when the oxide layer exceeded a thickness of 12 nm, the incidence of non-wetting solder joints increased exponentially.[3] Luo et al.[4] measured the surface oxide on Sn3.5Ag0.5Cu (SAC305) solder bumps by use of transmission electron microscopy, and found a thin surface oxide layer approximately 6 nm thick on the as-received solder bumps. After aging at

(Received April 8, 2014; accepted November 11, 2014; published online December 4, 2014)

150°C for 120 h, the oxide layer grew to 50 nm thick. The thickness of oxide on the solder bump was proportional to the square root of elapsed time.[3,4] In other studies, the surface oxide that formed on Sn4Ag0.5Cu particles mainly comprised Sn_2O and SnO.[5–7] As the oxide thickens, the solder coalesces more slowly.[5,8] As a consequence, the thicker oxide layer usually increases the reflow time and the soldering temperature required to establish an equivalent wetting angle. To slow the oxidation of micro bumps, a micro-alloying process was introduced for Pb-free solder. Common alloying elements for this purpose include Ge and P.[9–14]

In this work, we investigated the thermal residue stress and critical surface oxide thickness of the bumps. The stability of the oxide layer was first observed by use of a high-speed camera. Different thicknesses of surface oxide on heated solder micro-bumps were examined to determine the critical oxide thickness. A model of thermal residue stress of surface oxide on micro-bumps is discussed in detail.

EXPERIMENTAL

Solder micro bumps with a radius of 35 μm were used. The solder was Sn doped with 0.5 wt.% Cu. Some of the solder bumps from same box were heated to 150°C for up to 48 h. Every 12 h, several solder bumps were analyzed for surface oxide thickness. The oxide depth was profiled by use of Auger electron spectroscopy (AES) under a vacuum of 10^{-7} Torr during sputtering. The sputtering rate was approximately 2.2 nm/min, which was calibrated by use of a silica sample. Each measurement was recorded after a depth of 0.25 nm was reached. The accelerating voltage was 10 keV and the current was $I_p = 2 \times 10^{-8}$ A. The specimens were tilted at an angle of 30°. A total of five solder bumps were measured for each condition. After the oxide thickness was characterized, solder bumps with oxide layers 4.2 and 7.2 nm thick were placed on to a hot stage for reflow up to 250°C. Thermal profiles of solder bumps were collected by use of thermocouples. After reflow, the surface morphology of the solder bumps was examined by use of scanning electron microscopy. Solder bumps with oxide layers 7.2, 12.2, and 14.1 nm thick were used for *in situ* observation during reflow. At 200, 225, and 250°C, micrographs of the bump surface were recorded by use of a high-speed camera with a time resolution of 1 ms. The effect of temperature on oxide thickness on the bump surface were studied. The mechanical stability of the oxide layer on heating was then determined.

RESULTS

Figure 1 shows the typical AES depth profile of the solder bump. Surface oxide on the 35-μm solder bumps was sputtered by use of AES. The oxide layer was determined to be 4.2 nm thick on the basis of the intersection of the two slopes. The solder bump was then reflowed in a nitrogen environment with less than 50 ppm O_2. The solder bump was observed to have a smooth and round surface, as shown in Fig. 2a. We then reflowed a solder bump with a 7.2-nm oxide layer on the surface; Fig. 2b shows the surface morphology of the solder bumps after reflow. When the oxide layer was 7.2 nm thick, a crumpled bump surface was observed after reflow.

To understand the different surface morphology, bump surfaces with oxide layers of different thickness were inspected during reflow by use of a high-speed camera with 100× magnification. Figure 3a, b, and c show sequential micrographs of oxide layers 7.2, 12.2, and 14.1 nm thick, respectively, at 200°C, 225°C and 250°C. The micrographs show the progressive cracking of the oxide layer during reflow. When the oxide layer was 7.2 nm thick, the oxide shattered and separated upon melting, as shown in Fig. 3a. For the 12.2-nm-thick oxide layer, Fig. 3b shows that the oxide tended to fracture along cracks in the lining. The thermal stress energy was mostly consumed by fracture of the oxide surface, so there was less energy for shattering. With the 14.1-nm-thick oxide layer, the molten solder of the micro-bump was contained within the oxide layer, as shown in Fig. 3c. This observation is similar to the filling of a balloon with water. For the 14-nm-thick surface oxide layer on the solder bumps, a smooth solder bump surface was observed after the molten solder had cooled. Thus, increasing the thickness of the oxide layer on the solder bump produces an initially smooth surface; this then crumples and is followed by another smooth surface.

DISCUSSION

Thermal Stress Model of Surface Oxide on Spherical Micro-solder Bump

Thermal stresses and strains of the oxide generated during heating have been well researched for Si as substrate.[15–18] However, analysis of the surface oxide on soldered bumps is mostly based on

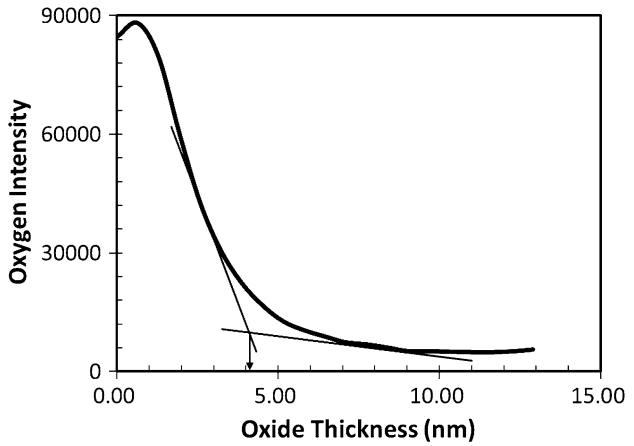

Fig. 1. AES depth profile of the 4.2-nm thick oxide layer on a 35-μm-radius solder bump. Thickness of the oxide layer was defined on the basis of the intersection of the two slopes.

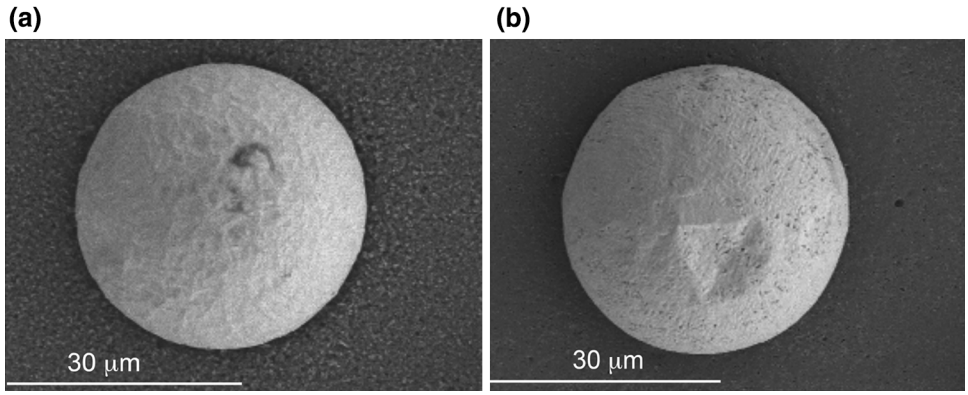

Fig. 2. Surface morphology of 35-μm-radius soldered bumps after reflow: (a) bump surface with 4.2-nm-thick oxide layer; (b) bump surface with 7.2-nm-thick oxide layer.

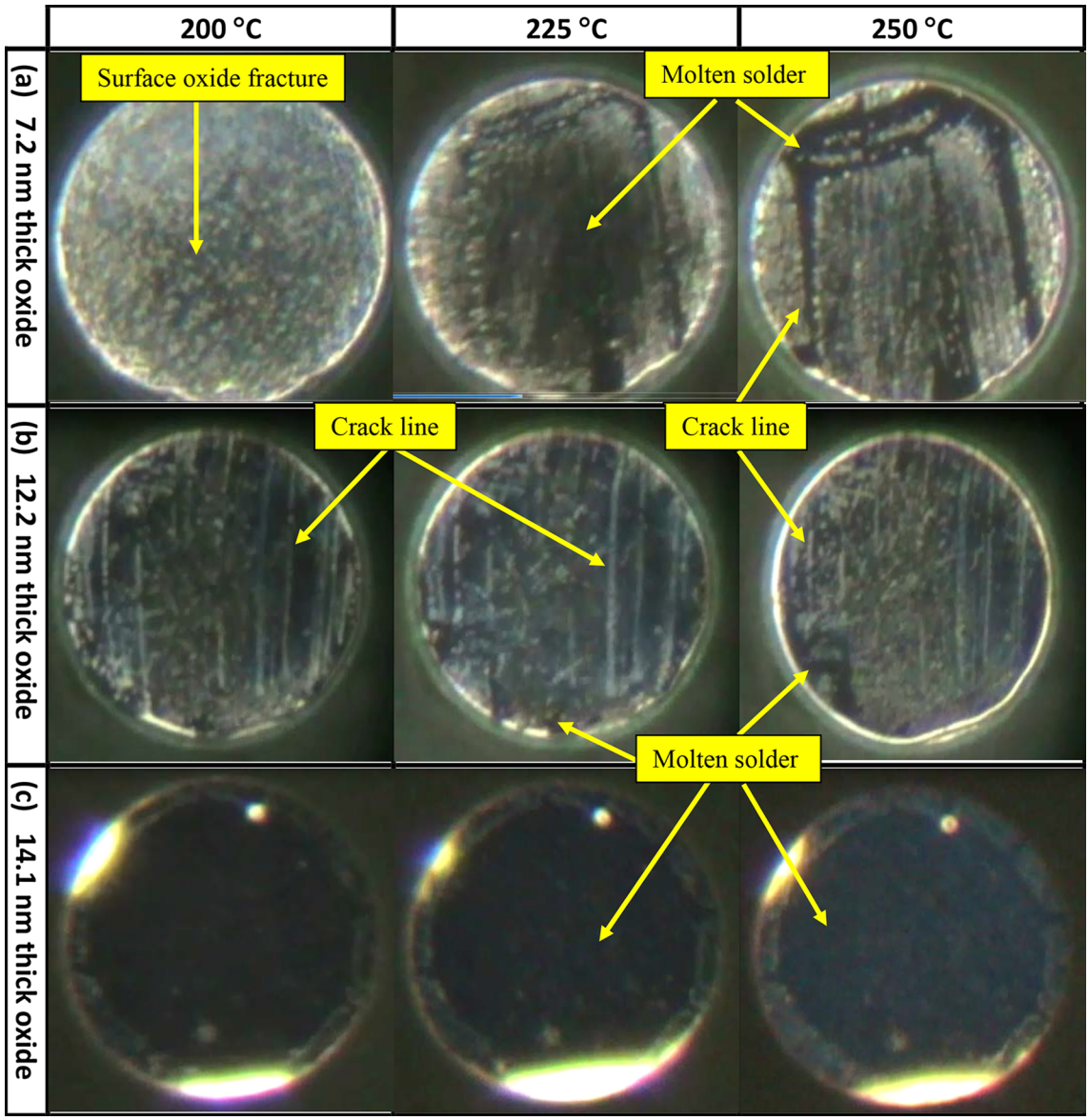

Fig. 3. Sequential micrographs of oxide layers 7.2, 12.2, and 14.1 nm thick on 35-μm-radius solder bumps during reflow at 200, 225, and 250°C.

wettability and observation.[5,8,19] To better explain above experimental results, we developed a thermal stress model for the surface oxide of a spherical micro-solder bump. A list of symbols is provided in Table I.

Several assumptions were made:

- A plane-strain condition was assumed. The strain of the entire oxide thickness was considered to be evenly distributed. The effects of plasticity and creep on both the oxide and metal were neglected. The tensile stresses were uniformly distributed over the oxide section, and the effects of the curvature of the spherical wall were neglected. The thickness of the oxide relative to the solder bump was too thin; thus, a biaxial stress model was applied.
- The oxide layer was assumed to be uniform and defect-free. Oxidation was based on anions and cations via thermal diffusion.

Table I. List of symbols

σ_L	Circumferential stress
σ_θ	Radial stress
A	Area of solder bump
r_o	Radius of solder bump
x	Thickness of oxide layer
P	Pressure
γ	Specific interfacial surface free energy
H	Reciprocal radius (mean curvature)
P_ε	Maximum pressure in the SnO film
P_v	Built-up pressure inside solder bump
t	Critical oxide thickness of solder bump
E	Young modulus of SnO_2
v	Poisson ratio
P_s	Pressure induced by thermal expansion of solid Sn
P_L	Pressure induced by thermal expansion of liquid Sn
P_m	Pressure induced by solder melting
P_{at}	Atmospheric pressure
β_O	Compressivity of oxide
α_0	Expansivity of solid oxide
β	Compressivity of solder
$\alpha_{sn(s)}$	Expansivity of solid solder
$\alpha_{sn(L)}$	Expansivity of liquid solder
$C_{O,P}$	Heat capacity of oxide at constant pressure
$C_{O,V}$	Heat capacity of oxide at constant volume
V	Spherical solder bump volume
T	Absolute temperature
r_o	Bump radius
T_o	Initial absolute temperature at solid stage for solder bump
T_s	Final absolute temperature at solid stage for solder bump
T_L	Absolute temperature at liquid stage for solder bump
T_m	Melting temperature for solder bump
ρ_s	Solid-state density of solder
ρ_L	Liquid-state density of solder
ρ_0	Density of oxide film
S_o	Tin oxide entropy
M	Molecular weight

- The oxide layer comprised only tin oxide (SnO and SnO_2) and was homogeneously distributed. The growth of oxide was negligible during the heating of the solder micro-bump because the heating time was within seconds and the oxygen concentration was below 50 ppm.
- The temperature gradient of the micro-bump was negligible as the dimensions were on the micron scale.

Consider a thin oxide layer on a spherical solder micro-bump as illustrated in Fig. 4; the stresses on the oxide layer can be balanced as:

$$\begin{aligned} P_\varepsilon &= P_v + 2\gamma H - P_{at} \quad \text{and} \quad H = \frac{2}{r_0} \\ P_\varepsilon &= P_v + 4\gamma/r_0 - P_{at} \\ P_\varepsilon &= P_s + P_m + P_L + \frac{4\gamma}{r_0} - P_{at} \end{aligned} \tag{1}$$

Each stress can then be derived individually.

Maximum Stress the Oxide Film Can Support, P_ε

When an oxide film on a spherical solder bump is heated, two types of stress develop: σ_L is compressive and in the tangential direction whereas σ_θ is tensile and in the radial direction. These stresses are at right angles to each other. The force acting on the oxide film is $P_\varepsilon r_o^2$; the area resisting this force is $2\pi r_o x$. For a thin oxide film, $r_0(\mu m) \gg x(nm)$; the stress applied to the thin oxide is $\sigma_\theta = \frac{P_\varepsilon r_o}{2x}$. Because the strain is isotropic, $\sigma_\theta = \sigma_L = \frac{P_\varepsilon r_o}{2x}$.

For radial elastic strain, $\varepsilon = \frac{dr}{r_o} \Rightarrow \frac{P_\varepsilon r_o}{2Ex}(1-v)$, and the volumetric strain is $\frac{dV}{V} = 3\varepsilon$. By substituting for ε:

$$\frac{dV}{V} = \frac{3P_\varepsilon r_o}{2Ex}(1-v) \tag{2}$$

Because $dV = V\alpha_O dT - V\beta dP$ and, $dP = \frac{1}{TV\alpha_O}[C_P dT - TdS]$,[20] Eq. 2 becomes:

$$\frac{dV}{V} = \alpha_O dT - \beta_O dP = \frac{3P_\varepsilon r_o}{2Ex}(1-v) \tag{3}$$

where V for the solid film can be expanded to $\frac{4}{3}\pi\left[(3r_0^2 x + 3r_0 x^2 + x^3\right]$. Again, $r_0 \gg x$; x^2 and x^3 are negligible, and $V = 4\pi r_0^2 x$. By replacing dP and V in Eq. 3:

$$\frac{3P_\varepsilon r_o}{2Ex}(1-v) = \alpha_O dT - \frac{\beta_O}{4\pi r_0^2 x \alpha_O T}[C_{O,P}dT - TdS] \tag{4}$$

where $[C_{O,P}dT - TdS]$ is in joules per mole per kelvin. Eq. 4 is converted to mass/molecular weight. For thin films to which the biaxial model is applied, the mass/molecular weight can be measured in the

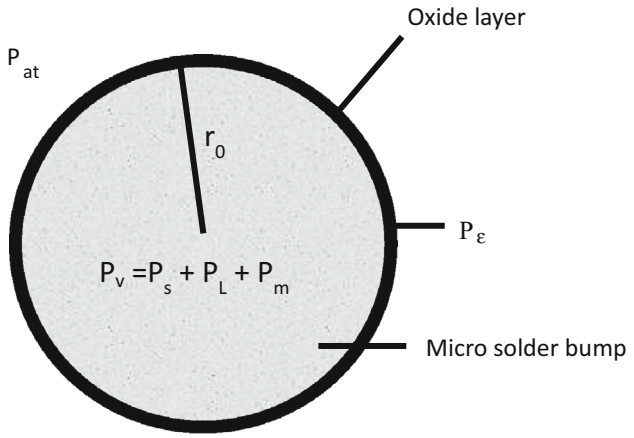

Fig. 4. Schematic diagram of surface oxide on a micro solder bump.

linear form $\frac{x\rho}{M}$.[20] By incorporating this factor, we obtain:

$$\frac{3P_{\varepsilon}r_{\mathrm{o}}}{2Ex}(1-v)=\alpha_{\mathrm{O}}dT-\frac{\beta_{\mathrm{O}}\rho}{4\pi r_{\mathrm{o}}^{2}T\alpha_{\mathrm{O}}M}[C_{\mathrm{O,P}}dT-TdS]$$

$$P_{\varepsilon}=\frac{2Ex}{3r_{\mathrm{o}}(1-v)}\left\{\alpha_{\mathrm{O}}dT-\frac{\beta_{\mathrm{O}}\rho}{4\pi r_{\mathrm{o}}^{2}T\alpha_{\mathrm{O}}M}[C_{\mathrm{O,P}}dT-TdS]\right\} \tag{5}$$

Stress Development on a Solder Bump Under Solid P_S and Liquid P_L

At constant volume, $dS=\frac{C_{\mathrm{P}}\partial T}{T}-V\alpha_{\mathrm{Sn}}dP$[20]; the integration produces $P_{\mathrm{s}}=\frac{1}{V\alpha_{\mathrm{Sn}}}\left[C_{\mathrm{p}}\ln\frac{T_{\mathrm{S}}}{T_0}-\Delta S\right]$ and $\Delta S=C_{\mathrm{v}}\ln\frac{T_{\mathrm{s}}}{T_0}$.[20] Then, $P_{\mathrm{s}}=\frac{1}{V\alpha_{\mathrm{Sn}}}\left(\ln\frac{T_{\mathrm{S}}}{T_0}\right)[C_{\mathrm{p}}-C_{\mathrm{v}}]$ and $C_{\mathrm{p}}-C_{\mathrm{V}}=\frac{TV\alpha_{\mathrm{Sn}}^{2}}{\beta}$[20]; hence:

$$P_{\mathrm{s}}=\left(\frac{T_S\alpha_{Sn(S)}}{\beta}\right)\left(\ln\frac{T_s}{T_0}\right)\quad\text{(solid)}\tag{6.1}$$

$$P_{\mathrm{L}}=\left(\frac{T_L\alpha_{Sn(L)}}{\beta}\right)\left(\ln\frac{T_L}{T_m}\right)\quad\text{(liquid)}\tag{6.2}$$

Stress Development on Solder Bump During Melting P_m

During melting, the temperature of the system is constant; the solder changes from the solid to the liquid state under the conservation of mass: $-\frac{dV}{V\beta}=dP, dV=m_{\mathrm{s}}\left(\frac{1}{\rho_{\mathrm{L}}}-\frac{1}{\rho_{\mathrm{s}}}\right)$, and $m_{\mathrm{s}}=V\rho_{\mathrm{s}}$. Combining these terms, we obtain:

$$dP=\frac{1}{\beta}\left[1-\frac{\rho_S}{\rho_L}\right]\tag{7}$$

By substituting the variables from Table II, we calculate $\frac{dV}{V_3}=34.29\times10^{-3}$. Harrison[21] obtained 23×10^{-3}, so the results are a good match.

Dependence on Thermal Stress of the Maximum Thickness of Oxide Film on the Solder Bump Allowing Formation of a Solder Joint

By substituting Eqs. 6.1, 6.2 and 7 into Eq. 1, we obtain the thermal stress equation:

$$P_{\varepsilon}=\left(\frac{T_{\mathrm{S}}\alpha_{Sn(S)}}{\beta}\right)\left(\ln\frac{T_{\mathrm{S}}}{T_{\mathrm{o}}}\right)+\frac{1}{\beta}\left[1-\frac{\rho_{\mathrm{S}}}{\rho_{\mathrm{L}}}\right]+\left(\frac{T_{\mathrm{L}}\alpha_{Sn(L)}}{\beta}\right)\times\left(\ln\frac{T_{\mathrm{L}}}{T_{\mathrm{m}}}\right)+\frac{4\gamma}{r_0}-P_{\mathrm{at}}\tag{8}$$

We then replace P_{ε} with Eq. 5 and rearrange the equation to obtain the maximum oxide thickness on the solder bump:

$$x=\frac{3r_{\mathrm{o}}(1-)}{2E\left\{\alpha_{\mathrm{O}}dT-\frac{\beta_{\mathrm{O}}\rho}{4r_{\mathrm{o}}^{2}T\alpha_{\mathrm{O}}M}[C_{\mathrm{O,P}}dT-TdS]\right\}}\times\left(\left(\frac{T_{\mathrm{S}}\alpha_{\mathrm{Sn(S)}}}{\beta}\right)\left(\ln\frac{T_{\mathrm{S}}}{T_{\mathrm{o}}}\right)+\frac{1}{\beta}\left[1-\frac{\rho_{\mathrm{S}}}{\rho_{\mathrm{L}}}\right]+\left(\frac{T_{\mathrm{L}}\alpha_{Sn(L)}}{\beta}\right)\times\left(\ln\frac{T_{\mathrm{L}}}{T_{\mathrm{m}}}\right)+\frac{4\gamma}{r_0}-P_{\mathrm{at}}\right)\tag{9}$$

This model can be used to determine the maximum oxide thickness on the solder bump which can still form solder joint.

Figure 5 shows the thermal stress of surface oxide when using Eq. 8 to analyze solder bumps of radius 35 μm under non-fracture oxide conditions. The values were obtained from the literature, and are listed in Table II. The figure shows that the thermal stress on the oxide film increased almost linearly with increasing temperature until the melting point. At the melting stage, the thermal stress suddenly increased rapidly because of the change of thermal expansion from solid to liquid with conservation of mass. Equation 9 is used to determine the maximum oxide thickness on a solder bump which supports the thermal stress. Figure 6 shows that, when the solder bump is in the solid state, the maximum oxide film is required to increase exponentially with increasing temperature. During reflow, the oxide thickness must increase abruptly, to support the change in thermal stress. Under natural conditions, the growth of oxide thickness on the solder bump depends on the square root of the elapsed time, with the temperature as an exponent.[3] Thus, the increased thermal stress will crack most of the oxide film on the solder bump unless a much thicker initial oxide layer is formed. Figure 6 suggests that for a bump of radius 35 μm a maximum oxide layer thickness of 14 nm is required to support thermal stress up to 250°C. By comparing to the

Table II. Variables of the thermal stress model

Symbol	Value	Ref.
$\alpha_{Sn\ (S)}$	$59.8 \times 10^{-6}\ K^{-1}$	Harrison[21]
$\alpha_{Sn\ (L)}$	$106 \times 10^{-6}\ K^{-1}$ (at 513 K)	Schramm[22]
ν	0.2	Clavette[23]
γ	$65.45 \times 10^{-3}\ J/m^2$	Saatci et al.[24]
β	$2.45 \times 10^{-11}\ Pa^{-1}$	Sharafat and Ghoniem[25]
ρ_s	$7.29\ gcm^{-3}$ (at 288 K)	Sharafat and Ghoniem[25]
ρ_L	$7.04\ gcm^{-3}$ (at 494 K)	Sharafat and Ghoniem[25]
α_o	$11.7 \times 10^{-6}\ K^{-1}$	Madelung et al.[26]
β_O	$4.5 \times 10^{-12}\ Pa^{-1}$	Madelung et al.[26]
ρ	$6.994\ g\ cm^{-3}$	Madelung et al.[26]
dS	$52.34\ J\ mol^{-1}\ K^{-1}$	Madelung et al.[26]
$C_{O,P}$	$52.59\ J\ mol^{-1}\ K^{-1}$ (at 300 K)	Madelung et al.[26]
M	150.708 g	Madelung et al.[26]
E	100×10^9 Pa	Barth et al.[27]
P_{at}	101,325.01 Pa	Wikipedia.org[28]

experimental results, the maximum thickness for the surface oxide layer of a solder bump with a radius of 35 μm is 14.1 nm. The results are a good match with the plot from the model. In addition, Fig. 6 suggests that the 7.2-nm-thick oxide layer on the solder bump can withstand the thermal stress in the solid state; this is found in Fig. 3. However, the oxide layer on the solder bump shattered into pieces during the melting process as the thermal stress on the solder bump increased abruptly. The shattered oxide fragments separated from each other, and the oxide pieces on the molten solder bump surface then hit each other upon cooling to form the crumpled surface on the solder bump in Fig. 2.

Figure 7 shows maximum oxide thickness as a function of temperature for solder bumps of different size before melting. The maximum oxide thickness was found to depend on the size and temperature of the solder bump. For a given bump radius, increasing the thickness of the oxide layer improves its resistance to thermal stress. For smaller bumps, only a thin oxide layer is required to support the thermal stress without cracking.

The results suggest that a thick oxide layer is likely to remain on the surface. The oxide layer separates the solder from the substrate, which results in a non-wetting solder joint, as reported elsewhere.[3,29] In accordance with the scaling trend of Si gate oxides, solder micro-bumps will continue to decrease in size to match performance. The stability of the surface oxide layer on solder bumps is expected to increase, leading to non-wetting solder joints. Therefore, determining the effect of thermal stress on the oxide film is essential for forming a good solder joint.

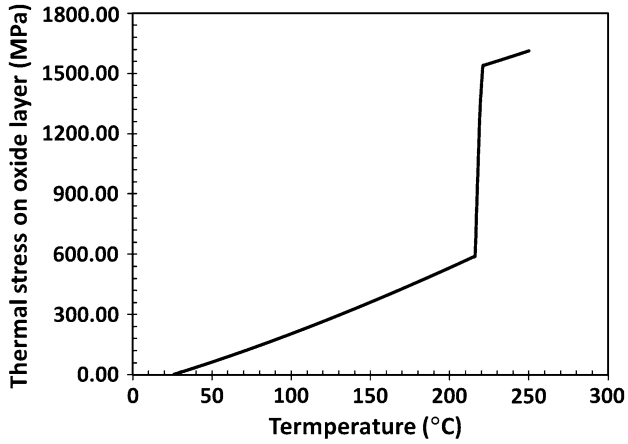

Fig. 5. Plot of thermal stress of surface oxide on the 35-μm radius solder bumps under oxide non-fracture conditions.

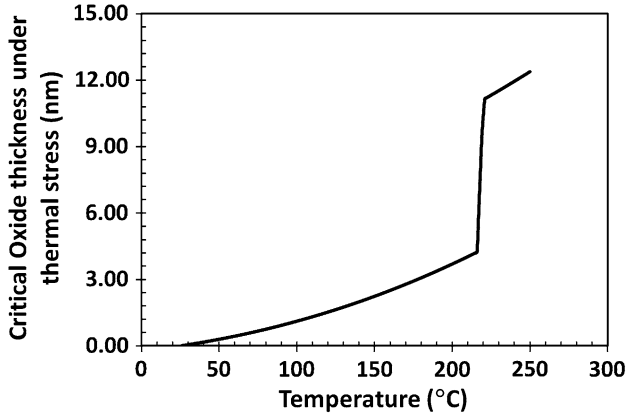

Fig. 6. Plot of critical oxide layer of the 35-μm-radius solder bumps as a function of temperature under oxide non-fracture conditions.

SUMMARY

We investigated thermal stress of the surface oxide layer on 35-μm micro bumps. After heating to 250°C, the bump with a 4.2-nm surface oxide layer had a smooth surface. However, bumps with a 7.2 nm oxide layer had a crumpled surface. The 7.2 nm oxide layer shattered during melting,

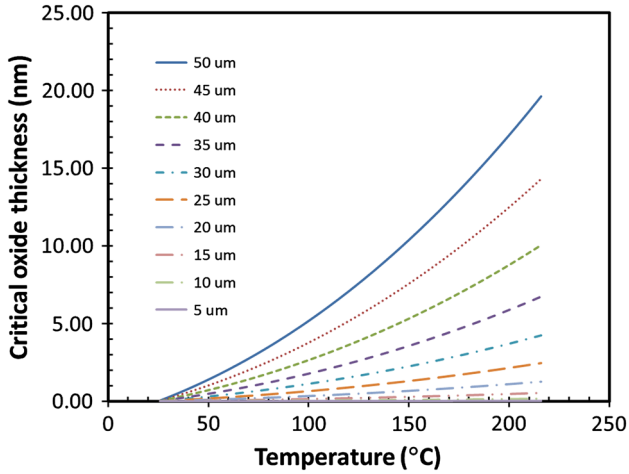

Fig. 7. Relationships among size of solder bump, temperature, and critical oxide thickness before melting.

because of increased thermal stress. When the oxide thickness was 12.2 nm, the oxide layer formed cracks along the lining rather than shattering. Most of the thermal stress energy was consumed in cracking of the oxide layer. Bumps with a 14.1-nm oxide layer were stable to heating even after reflow, and the solder bump had a smooth surface. The thermal stress developed by the thin oxide layer on solder bumps increases almost linearly with temperature until the melting point. Upon melting, the thermal stress increases abruptly, because of the higher thermal expansion of the solder from the solid to liquid state. Hence, it will crack most of the oxide film unless a much thicker oxide film is formed to support the thermal stress. The experimental results clearly demonstrate that a 14.1-nm oxide layer can support heating without cracking. This oxide thickness will lead to non-wetting solder joints. Thus, as the sizes and pitches of solder micro-bumps on Si dies continue to decrease, the effects of the oxide layer on the solder bump surface will become more prominent.

ACKNOWLEDGEMENTS

This work is supported by the National Science Council through grant NSC-101-2221-E-002-087-MY3 and by Intel Microelectronics Asia Ltd.

REFERENCES

1. R. Chanchani, *Materials for Advanced Packaging*, ed. D. Lu and C.P. Wong (Boston: Springer, 2009), pp. 4–27.
2. K.N. Tu, *Microelectron. Reliab.* 51, 517 (2011).
3. C.K. Chung, Y.J. Chen, C.C. Li, and C.R. Kao, *Thin Solid Films* 520, 5346 (2012).
4. X. Luo, W. Du, X. Lu, T. Yamaguchi, J. Gavin, L. Ye, and J. Liu, *IEEE International Symposium on Advanced Packaging Materials*, Xiamen, China October 25–28 (2011), pp. 73–79.
5. S. Zhang, Y. Zhang, and H. Wang, *J. Alloys Compd.* 487, 682 (2009).
6. S. Cho, J. Yu, S.K. Kang, and D.-Y. Shih, *JOM* 57, 50 (2005).
7. F.Y. Hung, H.-M. Lin, P.-S. Chen, T.-S. Lui, and L.-H. Chen, *J. Alloys Compd*. 415, 85 (2006).
8. J. Gorlich, C.C. Oberdorfer, D. Baither, G. Schmitz, C. Reinke, and U. Wilke, *J. Alloys Compd.* 490, 336 (2010).
9. M. Abtew and G. Selvaduray, *Mat. Sci. Eng. R* 27, 95 (2000).
10. C.M.L. Wu, D.Q. Yu, C.M.T. Law, and L. Wang, *Mater. Sci. Eng., R* 44, 1 (2004).
11. T. Laurila, V. Vuorinen, and M. Paulasto-Krockel, *Mater. Sci. Eng., R* 68, 1 (2010).
12. J. Zhou, D. Huang, Y.-L. Fang, and F. Xue, *J. Alloys Compd*. 480, 903 (2009).
13. M.A. Dudek and N. Chawla, *J. Electron. Mater.* 38, 210 (2009).
14. C.K. Chung, T.C. Huang, R. Shia, T.L. Yang, and C.R. Kao, *J. Alloys Compd.* 539, 57 (2012).
15. C.-H. Hsueh and A.G. Evans, *J. Appl. Phys.* 54, 6672 (1983).
16. S.M. Hu, *J. Appl. Phys.* 64, 323 (1988).
17. C.S. Rafferty and R.W. Dutton, *Appl. Phys. Lett.* 54, 1815 (1989).
18. C.-H. Hsueh and S. Lee, *J. Appl. Phys.* 91, 2760 (2002).
19. K.-S. Kim, K. Suganuma, J.-M. Kim, and C.-W. Hwang, *JOM* 56, 39 (2004).
20. R. DeHoff, *Thermodynamic in Materials Science*, 2nd edn. (New York: CRC Press Taylor & Francis, 2006), Chap. 4 and 12.
21. P.G. Harrison, *Chemistry of Tin*, ed. P.J. Smith (New York: Springer, 1998), pp. 1–9.
22. K.H. Schramm, *Z. Metallk.* 53, 316 (1962).
23. P.L. Clavette, *A Study of Tin Wisker Growth in Electronics* (MSc thesis, Mech. Eng. Rensselaer Polytechnic Institute, August 2009).
24. B. Saatci, S. Cimen, H. Pamuk, and M. Gündüz, *J. Phys.: Condens. Matter* 19, 326219 (2007).
25. S. Sharafat and N. Ghoniem, *Summary of Thermo-Physical Properties of Sn and its Compounds* (Uni. of California L.A., 2000), pp. 8–23.
26. O. Madelung, U. Rössler, and M. Schulz, *Tin Dioxide (SnO_2) Crystal Structure, Lattice Parameters, Thermal Expansion* (The Landolt-Börnstein database-Group III Condensed Matter, Vol III 17E, 17F-41C) Chap. T1.
27. S. Barth, C. Harnagea, S. Mathur, and F. Rosei, *Nanotechnology* 20, 115705 (2009).
28. http://en.wikipedia.org/wiki/Atmospheric_pressure.
29. C.K. Chung, Y.J. Chen, T.L. Yang, and C.R. Kao, *J. Electron. Mater.* 42, 1254 (2013).